ACS APPLIED MATERIALS & INTERFACES

Energy, Environmental, and Catalysis Applications

Establishing Ultra-Low Activation Energies for Lithium Transport in Garnet Electrolytes

Federico M. Pesci, Antonio Bertei, Rowena H Brugge, Steffen P. Emge, A.K. Ola Hekselman, Lauren E Marbella, Clare P. Grey, and Ainara Aguadero

ACS Appl. Mater. Interfaces, **Just Accepted Manuscript** • DOI: 10.1021/acsami.0c08605 • Publication Date (Web): 23 Jun 2020

Just Accepted

is published by the American Chemical Society. 1155 Sixteenth Street N.W., Washington, DC 20036

Establishing Ultra-Low Activation Energies for Lithium Transport in Garnet Electrolytes

Federico M. Pesci,[1*] Antonio Bertei,[2] Rowena H. Brugge,[1] Steffen P. Emge,[3] A. K. Ola Hekselman,[1] Lauren E. Marbella,[4] Clare P. Grey[3] and Ainara Aguadero[1*]

1. Department of Materials, Imperial College London, London, SW7 2BP, UK

2. Department of Civil and Industrial Engineering, University of Pisa, 56122, Pisa, Italy

3. Department of Chemistry, University of Cambridge, Cambridge, CB2 1EW, UK

4. Department of Chemical Engineering, Columbia University, New York, NY 10027, USA

*Email: f.pesci@imperial.ac.uk, a.aguadero@imperial.ac.uk

Keywords

Garnet electrolytes, LLZO, activation energy, solid state batteries, electrochemical impedance spectroscopy, ssNMR, grain boundary

Abstract

Garnet-type structured lithium ion conducting ceramics represent a promising alternative to liquid-based electrolytes for all-solid-state batteries. However, their performance is limited by their polycrystalline nature and the inherent inhomogeneous current distribution due to the different ion dynamics at grains, grain boundaries and interfaces. In this study we use a combination of electrochemical impedance spectroscopy, distribution of relaxation times analysis and solid state nuclear magnetic resonance (NMR), in order to understand the role that bulk, grain boundary and interfacial processes play in the ionic transport and electrochemical performance of garnet based cells. Variable temperature impedance analysis reveals the lowest activation energy for Li transport in the bulk of the garnet electrolyte (0.15 eV), consistent with pulsed field gradient NMR spectroscopy measurements (0.14 eV). We also show a decrease in grain boundary activation energy at temperatures below 0 ˚C, that is followed by the total conductivity, suggesting that the bottleneck to ionic transport resides in the grain boundaries. We reveal that the grain boundary activation energy is heavily affected by its composition that, in turn, is mainly affected by the segregation of dopants and Li. We suggest that by controlling the grain boundary composition, it would be possible to pave the

way towards targeted engineering of garnet-type electrolytes and ameliorate their electrochemical performance in order to enable their use in commercial devices.

Introduction

Growing efforts to reduce CO_2 emissions have led to an increased interest in researching renewable sources of energy and developing energy storage systems capable of meeting the requirements for their application in electric vehicles, aerospace, and large-scale energy storage applications. Current lithium ion technologies provide volumetric and gravimetric energy densities up to 770 Wh L^{-1} and 260 Wh kg^{-1}, respectively;[1] however, in order to be employed in electric vehicles and grid applications, these values need to be increased and longevity and safety must be improved.[2,3]

In addition to increased safety, the replacement of currently used liquid electrolytes with a solid ionic conductor could enable the use of lithium metal as an anode, increasing the cell theoretical capacity by an order of magnitude and resulting in greater energy and power densities.[4]

Garnet-type solid electrolytes with general formula $Li_7La_3Zr_2O_{12}$ (LLZO) have attracted increasing interest in recent years as suitable candidates for the development of all-solid-state-batteries (ASSB) because of their high ionic conductivity at room temperature (up to 1 mS cm^{-1} for cubic LLZO)[5] and their electrochemical stability against lithium metal anodes. Stabilisation of the cubic LLZO phase has been achieved by several groups by donor-doping which optimises the conductivity in the lattice by tuning the content of lithium and subsequently the Li vacancy concentrations.[6] One of the most commonly studied garnet compositions is Ga-doped LLZO, $Li_{6.55}Ga_{0.15}La_3Zr_2O_{12}$, due to its ionic conductivity being amongst the highest reported in the literature,[7] coupled with its good reduction stability against lithium metal, making it a promising candidate for commercial implementation in solid state batteries.[8–10]

Although garnet electrolytes are in theory suitable candidates for ASSB, several problems still prevent their use in practical devices, including the formation of lithium dendrites at current densities as low as 0.3 mA cm^{-2},[11–13] and high charge transfer resistances at the electrode/electrolyte interfaces.[14,15] In particular, numerous reports have been published on the high Li/LLZO interfacial

resistance, how it affects the electrochemical cyclability of LLZO based cells and how to mitigate this effect. [11,16–21] It is widely recognised that, if exposed to moisture, LLZO can react with water to form lithium hydroxide (Eq. 1) and concomitantly react with CO_2 to form Li_2CO_3 (Eq. 2) and $LiHCO_3$ which, if present on the LLZO surface at the time of cell assembly, can lead to poor wetting of the LLZO surface by Li, resulting in very high polarisation resistances.[11,22–24]

$$Li_{6.55}Ga_{0.15}La_3Zr_2O_{12} + xH_2O \rightarrow H_xLi_{6.55-x}Ga_{0.15}La_3Zr_2O_{12} + xLiOH \quad \text{Equation 1}$$

$$2LiOH + CO_2 \rightarrow Li_2CO_3 + H_2O \quad \text{Equation 2}$$

It has been reported by several groups that a decrease of the interfacial resistance could be achieved by approaches such as surface treatment of LLZO electrolyte,[11,16] the use of interlayers between LLZO and the metallic Li, [17,25,26] and the application of high pressure at the electrolyte/electrode interface.[19,20,26] The effect of Li^+/H^+ exchange in the total conductivity and H-diffusion in garnet materials has been previously reported, [19] however the effect of this exchange in the Li mobility remains unclear and might be the source of some of the incongruences in the literature.

Although LLZO has been widely investigated in the past few decades as a suitable electrolyte for solid state lithium metal batteries, a well-established understanding of its ion transport properties and the contribution that bulk, grain boundary and electrode/electrolyte interfaces play in the overall conductivity of LLZO is still uncertain. A systematic study of its electrochemical properties using electrochemical impedance spectroscopy (EIS) coupled with an accurate interpretation of their spectra is therefore of pivotal importance in order to univocally define the transport properties of bulk, grain boundaries and electrode/electrolyte interface; this has been achieved in this study by analysing several LLZO pellets under different conditions. Several previous studies have reported the value of activation energy for both Al- and Ga-doped LLZO (referred as Al-LLZO and Ga-LLZO hereafter), and the general trend is a decrease in activation energy (E_a) when Ga is used instead of Al to stabilise the LLZO cubic phase. For example, Rettenwander et al. have investigated the effect of Al and Ga co-substitution in LLZO, reporting a change in E_a from 0.31 eV to 0.26 eV when LLZO is uniquely doped with Al or Ga, respectively.[27]

Zhang et al. have reported different activation energies for Al-LLZO which depend on the synthesis route - specifically they observed values of 0.41 eV and 0.26 eV for sol-gel and solid-state synthesised LLZO, respectively.[28] Although the ionic conductivity was the same for both samples, the change in activation energy was attributed to the differences in the pellet microstructure. They suggested that the nano-scale grain boundaries in sol-gel-prepared LLZO gave rise to unique transport properties that were more sensitive to temperature when compared to LLZO prepared by a solid-state route. This study suggests the importance that grain boundaries could have in determining the total energy barriers to ion transport in LLZO. Murugan et al. also reported an E_a for Al-LLZO synthesised via a solid-state route of 0.32 eV and suggested that the charge transfer across individual grain boundaries occurred with the same activation energy as the transport inside the bulk of the grains in the temperature range 18–300 °C.[29] Tanhaeff et al. have attempted a systematic EIS study in order to resolve the grain boundary and lattice impedance of hot pressed Al-LLZO, however they observed a process occurring at medium/low frequencies which they could not assign to any specific process.[30]

EIS is a powerful technique which is generally employed in order to determine the ionic mobility in various regions of solid electrolytes, including bulk, grain boundaries and interfaces with electrodes.[31] The polycrystalline nature of LLZO electrolyte, combined with the overlapping EIS features assigned to bulk and grain boundary due to their close values of capacitance, could lead to misinterpretation of the impedance spectra. Different microstructural features of LLZO electrolytes including grain size, grain boundary thickness and density, presence of secondary phases, moisture induced degradation and intrinsic conductivities of single grains within the pellet, could result in very different impedance spectra and a spread of values of resistances and capacitances. This inevitably leads to a non-trivial comparison of data reported in the literature, potentially creating confusion and sometimes contradictory conclusions within the scientific community. A systematic study is therefore needed in order to fully separate and understand the governing resistances and capacitances of LLZO. In this work we employ EIS with a high frequency (up to 13 MHz) impedance analyser to measure Ga-LLZO across a range of temperatures and conditions to univocally assign bulk, grain boundary and interfacial processes. We synthesise Ga-LLZO in a controlled atmosphere in order to avoid any

degradation process arising from air exposure possibly leading to the appearance of overlapping features in EIS spectra. The EIS analysis is assisted by the use of distribution of relaxation times (DRT) analysis, which deconvolutes EIS spectra through an infinite chain of resistance-parallel-capacitance (R//C) circuit elements in order to identify the individual processes according to their different time constants.[32,33] Solid-state NMR spectroscopy and diffusivity measurements were used to confirm the activation energies obtained for the bulk processes in several different garnet electrolytes. By comparing and combining EIS data with DRT studies, we could separate and estimate the importance of individual processes on the ionic transport of LLZO electrodes and provide insights into the role that bulk and grain boundaries play in the total activation energy of Ga-LLZO.

Results and Discussion

Ga-LLZO pellets with nominal composition $Li_{6.55}Ga_{0.15}La_3Zr_2O_{12}$ were synthesised using a sol-gel method as described in previous publications.[7] The uniaxially pressed and sintered pellets were finely polished (see Experimental Section for details) and the density was geometrically calculated to be between 96% and 98% of the theoretical density. Planar (Figure 1a) and cross sectional (Figure 1b) secondary electron micrographs (SEM) of thermally etched samples show a homogeneous surface of the pellets composed of tightly packed grains (very few internal pores are observed) with lateral dimensions ranging from 100 to 400 μm. The darker regions along the grain boundaries in Figure 1a are ascribed to be due to the fast reaction of the surface of the Ga-LLZO pellet with moisture when the samples were briefly exposed (less than one minute) to air during transfer from the Ar filled glove box (where the samples are synthesised and processed) to the SEM chamber. This highlights the importance of handling LLZO in a controlled atmosphere to minimise the contact with moisture, which we have previously shown to have a detrimental effect on the ionic transport properties of LLZO.[22]

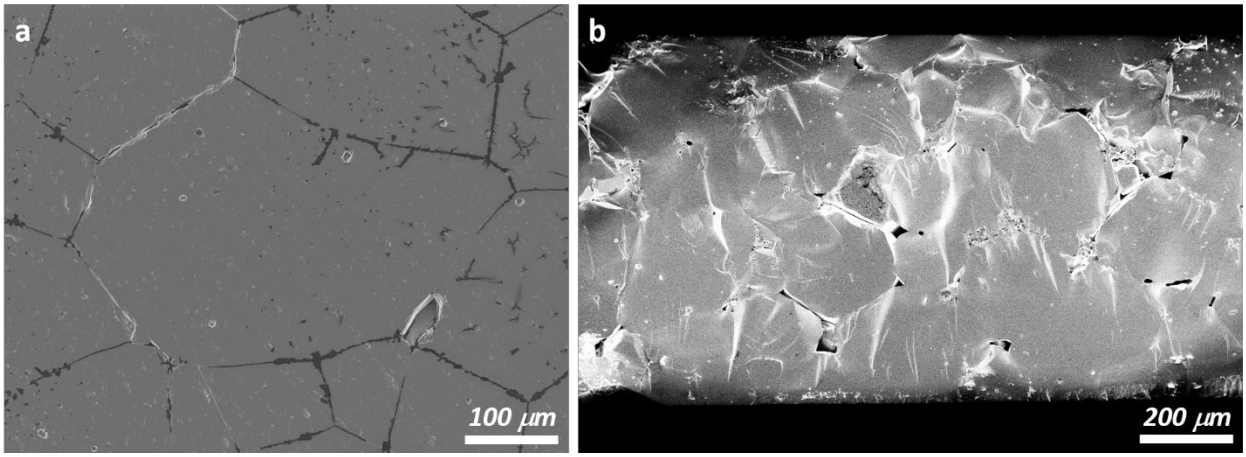

Figure 1. Planar (a) and cross sectional (b) SEM images of a Ga-LLZO pellet with a relative density of 97% showing a lateral grain size of several hundred μm.

Rietveld refinement of the X-ray diffraction pattern[34] indicates that the samples are pure and that they can be assigned to a cubic crystal structure with the $Ia\bar{3}d$ space group, shown in Figure S1.

In this study, the cubic structure was stabilised by Ga doping which leads to ionic conductivities three orders of magnitude higher than the tetragonal counterpart.[5,6]

In order to simplify interpretation of the EIS spectra, symmetrical cells with cold-pressed Li metal foil electrodes (kept at 1 MPa pressure by the coin cell spring for a pellet of 1 mm thickness)[35] were assembled using thermally etched samples. It has been recently observed that thermal etching leads to a substantial decrease in the interfacial resistance between LLZO pellets and metallic lithium.[11,16] After cell assembly and conditioning the cell without cycling, the resistance associated with the process occurring at low frequency decreases, indicating a stabilisation (conditioning) of the cell (Figure 2), possibly due to improved contact between the metallic lithium and the solid electrolyte over time as a result of the pressure exerted by the coin cell spring. However, the possibility of the formation of a stable and more ionically conductive dynamic interphase cannot be ruled out. The timescale for this stabilisation period spans the first 24 h after cell assembly, after which the cell does not show any further decrease in total resistance.

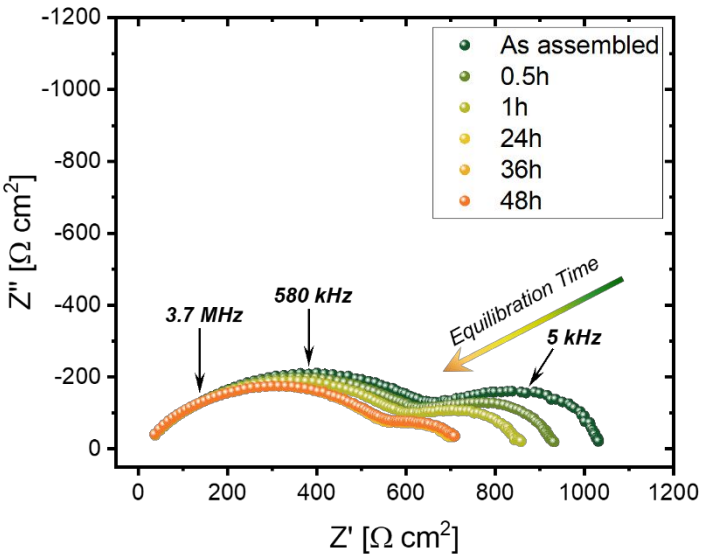

Figure 2. Electrochemical impedance spectra of a Ga-LLZO pellet recorded in the frequency range 13 MHz-1 Hz at different times following cell assembly.

Kramers-Kronig validity tests were carried out on the EIS spectra in order to verify the quality of the data and test the stability of the electrochemical system during the measurements.[36–38] In

Figure S2, the residuals from the Kramers-Kronig analyses are below 1% across the whole frequency range, indicating a good stability of the symmetrical cells; however, a further improvement of the residuals at longer times after cell assembly can be observed. This results in a better match between the real and imaginary residuals, most apparent after 24h, indicating an enhancement of the chemical and electrochemical stability of the cell over time, and serves to better facilitate the fitting process of the components of the impedance spectra to an equivalent circuit.

In order to select a suitable equivalent circuit to fit the EIS data, DRT analysis was carried out. Three main processes were identified at mid-to-high frequencies indicated by the numbers 1, 2 and 3 and attributed to bulk, grain boundary and electrode/electrolyte interface, respectively (Figure 3). The shift of peak number 3 to lower time constants during conditioning can be attributed to the decrease of interfacial resistance and thus a faster charge-transfer process. Additionally, two overlapping processes may contribute to peak number 3, indicating either a possible asymmetry of the two lithium electrodes, which can individually contribute to the DRT spectrum, or to two distinct contributions at the interface caused by features such as the constriction resistance and gap capacitance due to the presence of voids and to the resistance to ion transfer across the interface. The weakening with time of one of the processes could suggest an improved wetting between the Li metal and the garnet electrolyte. A decrease in the intensity of peak number 2 could be explained either with an improved contact between the grain boundaries sitting at a different height to the grain surface and the metallic lithium or a chemical interaction between grain boundaries and Li, which however could

not be defined in this study.

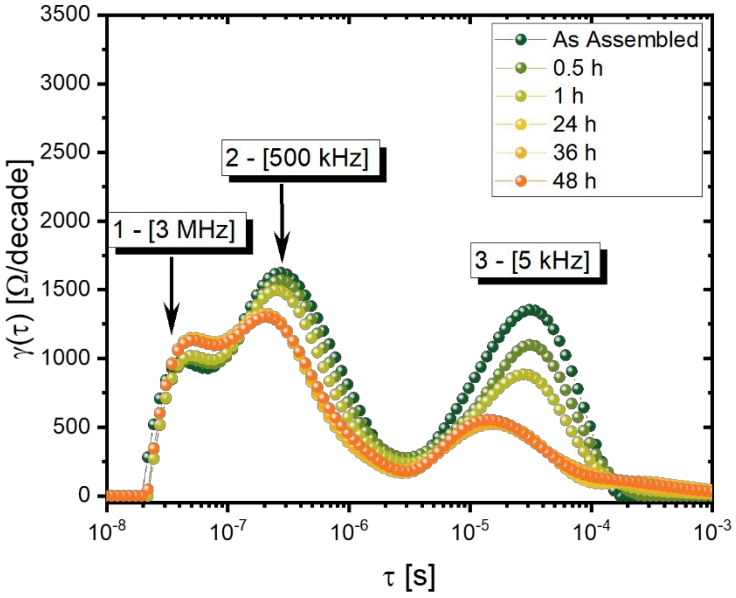

Figure 3: DRT analysis plot corresponding to the impedance spectra in Figure 2, carried out on a symmetric cell of Ga-LLZO at different times following cell assembly. Three distinct peaks are visible, indicating three different physical phenomena associated to bulk (1), grain boundary (2) and interfacial processes (3).

Following DRT analysis, which suggested the presence of three main processes, the spectra were fit using a combination of three R//CPE elements in series (where R is a resistor and CPE a constant phase element) to describe bulk, grain boundary and interfacial processes as described in Scheme 1:

Scheme 1: Equivalent circuit for EIS fitting

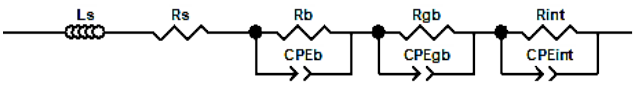

Scheme 1

L_s is the inductance of the system wiring, R_s, R_b, R_{gb} and R_{int} are resistances for the system wiring, bulk, grain boundary and interface, respectively and CPE_b, CPE_{gb} and CPE_{int} are constant phase elements for bulk, grain boundaries and interfacial processes. From the fitting of the EIS spectra shown in Figure 2, it was possible to calculate the corrected values of both resistance and capacitance for bulk, grain boundaries and interface with electrodes (Table 1). Capacitance values (C) were calculated from the CPE values using the fit parameters Q and n described by Equation 3:

$$C = \frac{(Q \cdot R)^{1/n}}{R} \qquad \text{Equation 3}$$

From the fittings of the EIS spectra reported in Table 1, the resistance and capacitance values associated with bulk and grain boundary processes do not vary more than a few percentage points across different measurements, indicating a good stability of the Ga-LLZO pellet. Conversely, the resistance values associated with electrode-electrolyte charge transfer decrease with stabilisation time, whereas the capacitance values slightly increase, indicating an improvement in the interface between solid electrolyte and electrodes as recently reported by Krauskopf *et al.*[20] who showed that a degradation in the interfacial contact due to voids leads to a decrease of the associated capacitance.

Table 1. Fitting results for the EIS spectra of a Ga-LLZO pellet enclosed in a symmetrical cell setup with Li metal electrodes, recorded at different times following cell assembly. The numbers in brackets indicate the % error calculated from the fitting of the spectra.

	R_b (Ω cm)	C_b (F)	R_{gb} (Ω cm)	C_{gb} (F)	R_{int} (Ω cm^2)	C_{int} (F)
As Assembled	1160.5 (6%)	5.6x10^{-11} (3%)	4778.0 (2%)	1.5x10^{-10} (9%)	208.9 (3%)	1.9x10^{-8} (12%)
1 h	916.0 (6%)	1.1x10^{-11} (2%)	4614.4 (4%)	1.5x10^{-10} (4%)	155.3 (6%)	1.8x10^{-8} (9%)
24 h	844.6 (3%)	9.7x10^{-11} (3%)	4774.8 (6%)	2.6x10^{-10} (3%)	99.23 (3%)	2.3x10^{-8} (5%)
48 h	1052.8 (9%)	6.69x10^{-11} (3%)	4730.6 (2%)	1.3x10^{-10} (2%)	92.1 (3%)	2.6x10^{-8} (3%)

Table 1 shows that the C_b and C_{gb} values match well the capacitances for bulk and grain boundary processes described by Irvine *et al.* (10^{-11} and 10^{-10} F, respectively).[31] However, the capacitance values associated with the Ga-LLZO-electrode interface (10^{-8} F) do not, and in the literature are generally associated either with grain boundaries or a surface layer.[31] However, our DRT analysis suggests that we are looking at three main processes which can be described as bulk, grain boundary and electrode-electrolyte interface.

In order to confirm the assignment of the different process, further measurements were performed. First, a symmetrical cell with sputtered gold blocking electrodes was measured. DRT analysis, Figure 4a, shows the presence of two well-separated processes at high-to-medium frequencies, suggesting that we are looking at bulk and grain boundaries. In accordance with DRT

analysis, it was possible to fit the first semicircle in the Nyquist plot by using two R//CPEs analogous to our previous assignment (Figure 4b).

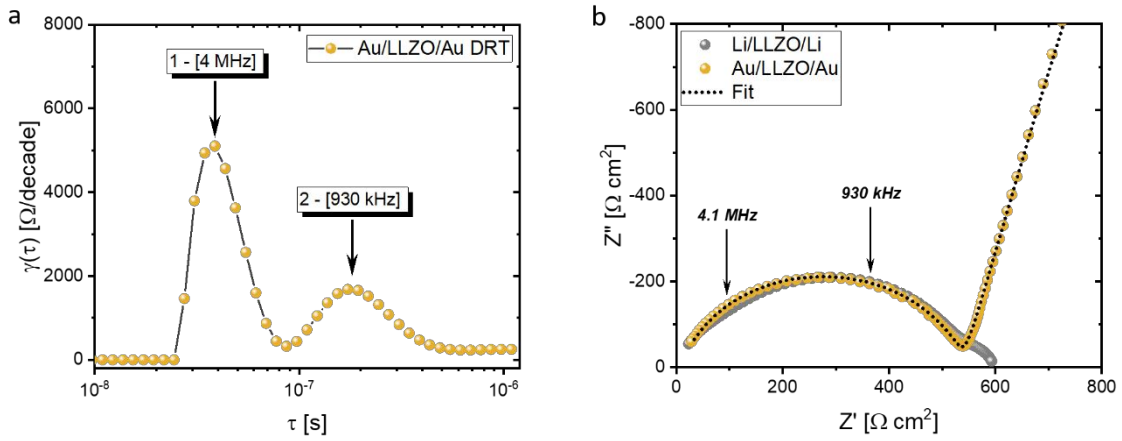

Figure 4. a) DRT analysis plot and b) corresponding EIS spectra recorded for a Ga-LLZO pellet enclosed in a coin cell with Au electrodes (yellow circles) compared to the EIS spectrum with lithium electrodes (grey circles). Solid circles represent the experimental data and dotted line the fitting.

From the fitting of the spectrum in Figure 4b, the values of capacitance for bulk and grain boundary were calculated to be 3.6×10^{-11} F and 7.9×10^{-11} F, respectively, in good agreement with the values previously calculated for Li/LLZO/Li symmetric cells shown in Table 1.

Second, a thickness-dependent measurement was performed to validate processes affected by the bulk thickness of the pellet as being separate from interfacial phenomena. EIS was performed on a thick (1.2 mm) Ga-LLZO with symmetric Li electrodes (Figure 5). After removing the pellet and grinding down to more than half of the original thickness (0.5 mm), the cell was re-assembled and measured again with EIS. Using the same pellet permitted the reasonable assumption of identical bulk and grain boundary contributions for the two measurements when the data are normalised by electrode area and pellet thickness (Figure 5a). From Figure 5a, it is indeed clear that the first semicircle which we assign to combined bulk and grain boundary contributions remains almost unvaried upon area and thickness normalisation, whereas the electrode/electrolyte interface resistance appears larger for the thinner pellet. The interface transport processes should be independent of the pellet thickness, therefore, if the interfacial resistance is divided by the thickness, the thinner pellet will show a higher normalised value of resistance. On the other hand, by normalising by the area only,

the interfacial resistance semicircles should superimpose well for both samples, whereas the first semicircle would not, as shown in Figure 5b. The results of the fitting of the two EIS spectra are reported in Table 2.

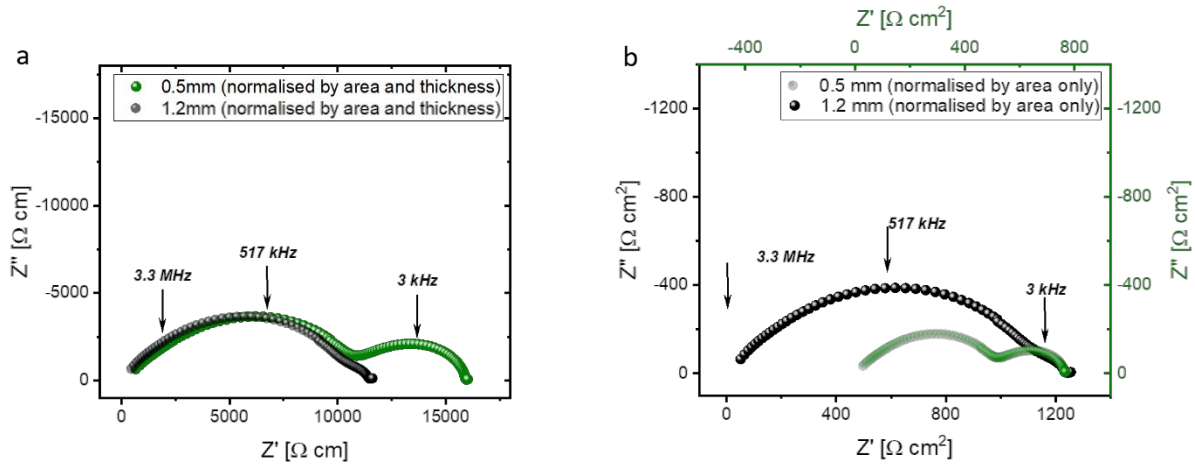

Figure 5. a) EIS spectra recorded for a thick (1.2 mm, black dots) and thinned down (0.5 mm, green dots) Ga-LLZO pellet across the frequency range 13 MHz to 1 Hz and normalised by electrode area and pellet thickness. b) EIS spectra of the same sample normalised by electrode area only.

Table 2. EIS fitting results for a thick (1.2 mm) and a thin (0.5 mm) Ga-LLZO pellet measured in a symmetric Li/LLZO/Li cell. The numbers in brackets indicate the % error calculated from the fitting of the spectra.

	R_b (Ω cm)	C_b (F)	R_{gb} (Ω cm)	C_{gb} (F)	R_{int} (Ω cm²)	C_{int} (F)
1.2mm LLZO	1320 (1%)	7.6×10^{-12} (1%)	7961 (3%)	1.4×10^{-11} (1%)	71 (2%)	1.1×10^{-8} (6%)
0.5mm LLZO	1729 (2%)	7.8×10^{-12} (2%)	9025 (1%)	3.9×10^{-11} (6%)	126 (1%)	2.6×10^{-8} (7%)

Table 2 shows that the values of capacitance and resistance for the bulk and grain boundaries are the same order of magnitude for both thin and thick pellets. The discrepancy between the values is ascribed to variability in the fitting parameters. The interfacial resistance also differs slightly, and this is ascribed to the variability in the preparation of the symmetrical cells, namely the variation in surface roughness resulting from the hand-polishing technique used. EIS analysis of the same sample with different thickness therefore confirms the assignment of the interfacial resistance process;

however, the separation of bulk and grain boundary contributions to the impedance spectra need further exploration.

Third, we carried out EIS analysis on a pre-conditioned cell at low temperatures, down to -100 °C, at which all the transport processes are slower (occurring at lower frequencies), allowing for a proper assessment of the bulk conductivity and an easier identification of the two high-to-mid frequency processes. Impedance was measured between -100 °C and +75 °C. As expected, the total resistance of the cell increases with decreasing temperature as the Li ion mobility decreases (Figure 6a). This, however, helps in the deconvolution of grain and grain boundary contributions. Figure 6b shows a magnification of the high frequency region of two impedance spectra recorded at -100 °C and -75 °C. It is possible to see that, at higher frequencies, there is the appearance of a better resolved feature (grey area) that we attribute to the bulk contribution. It is important to note that the characteristic frequencies reported in the figure are lower than the ones expected at room temperature due to the reduced mobility of Li ions at low temperatures.

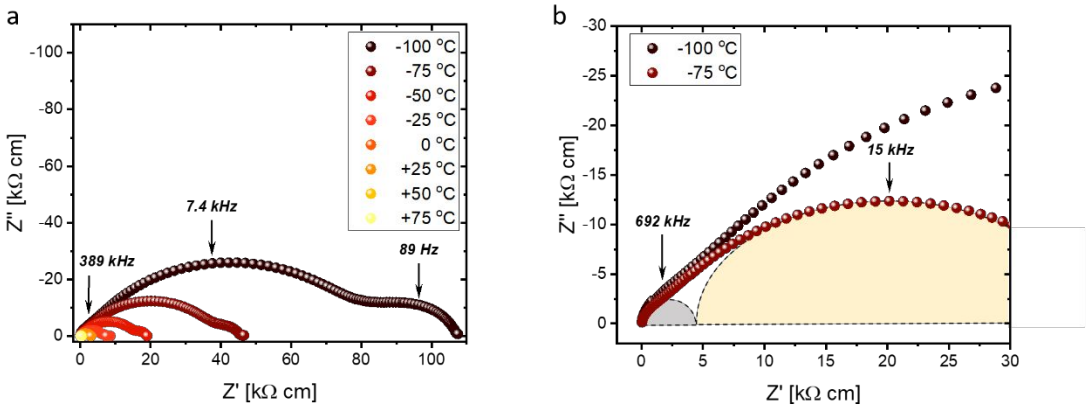

Figure 6. EIS spectra recorded for a thermally etched Ga-LLZO pellet a) between -100°C and +75°C, where the frequency markers refer to the -100°C spectrum. b) Magnification of the high frequency region showing the separation of the bulk contribution (grey area) and grain boundary (yellow area) at low temperatures; the frequency markers refer to the -75°C spectrum.

DRT analysis was carried out prior to performing the fitting of the spectra. The DRT spectra reported in Figure S3 show three main features which are broader at lower temperatures, possibly due to slowing down of the transport processes. The DRT analysis shows that, when comparing bulk and grain boundary peaks, the grain boundary peak decreases significantly as temperature increases from

0 °C to 75 °C, indicating that the grain boundary resistance is highly sensitive to thermal activation for temperatures above 0 °C. On the other hand, for temperatures below 0 °C, both bulk and grain boundary peaks become larger in magnitude, but their area ratio remains almost constant, suggesting that bulk and grain boundary resistances have similar temperature-dependences below 0 °C.

The fitting of the impedance spectra was performed using the equivalent circuit described earlier in the text. Temperature dependent EIS measurements were carried out for several sets of samples and the results were consistent and reproducible (in Table S1 are reported the values of E_a for 5 representative samples). It is worth noting that the interfacial resistance at +75 °C is over three time lower than at room temperature, suggesting a better wetting of lithium on the LLZO surface. From the fitting of the recorded spectra it was possible to calculate the total, bulk and grain boundary conductivities (Figure 7a) and their relative activation energies reported in the Arrhenius-type plots for Li conductivity (Figure 7b, c and d, respectively). The activation energy for interfacial charge transfer was also calculated for a polished and thermally etched sample, showing similar values and indicating that the interfacial processes are not affected by surface treatments (Figure S4).

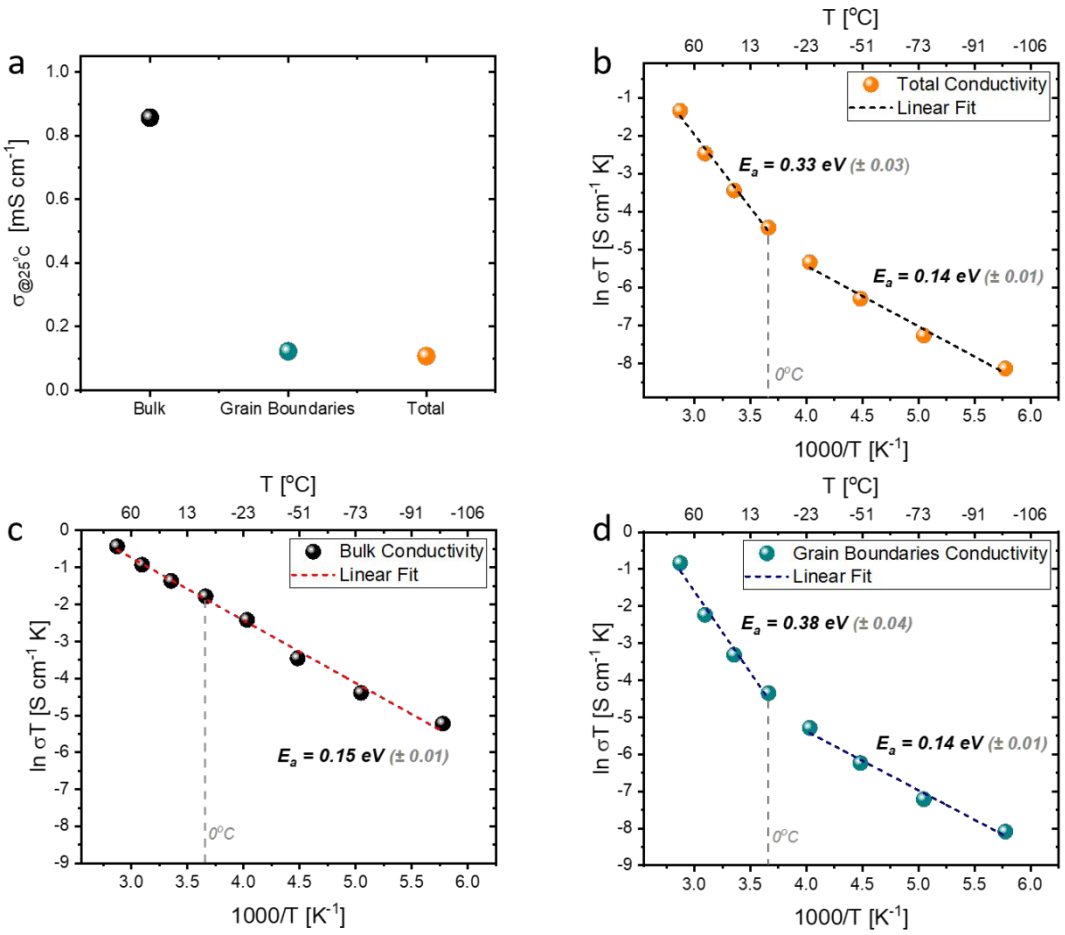

Figure 7. a) Bulk, grain boundary and total conductivity values and Arrhenius plots for b) total, c) bulk and d) grain boundary conductivity in Ga-LLZO.

A single value for the activation energy of the bulk material (E_a = 0.15 eV) is found across the entire temperature range examined (Figure 7c), whereas the activation energy for the grain boundaries changes at 0 °C (from 0.14 eV below 0 °C to 0.38 eV above 0 °C, Figure 7d), indicating a possible change in ionic transport mechanism. Above 0 °C, the total LLZO activation energy has a similar value to the grain boundary activation energy (E_a = 0.33 eV, Figure 7b).

To the best of our knowledge there has not been any report of a change in activation energy in LLZO electrolytes. To separate contributions from the bulk and grain boundaries using a different technique, bulk-sensitive ^{7}Li pulsed field gradient (PFG) NMR measurements were performed. For these experiments, ^{7}Li self-diffusion coefficients were measured at several temperatures between 180 and 120°C for Ga-LLZO as well as Al- LLZO. Ga-LLZO showed overall much higher diffusion coefficients, by around one order of magnitude. Fitting the data in an Arrhenius Plot (Figure 8) yields

a bulk activation energy (0.14 eV) for Ga-LLZO powders, in close agreement with the bulk value found in EIS, suggesting that we correctly assigned the bulk process in the impedance spectra. Figure 8 also shows that the bulk activation energy can be strongly dependent on the dopant used to stabilise the cubic phase, as an example, Al-LLZO has an E_a more than double that of Ga-LLZO. This activation energy of 0.32 eV is in line with the one measured via EIS for a pellet with density and microstructure comparable with Ga-LLZO (0.25 eV, see Figure S6) and the variation here is attributed to a slight difference in sample composition and to the fact that Figure 6 shows the total conductivity rather than bulk conductivity. (the PFG sample was only lightly doped via Al^+ diffusion from the Al_2O_3 crucible while EIS sample was intentionally Al-doped using an Al-precursor as a starting material in the synthesis). PFG-NMR measurements are expected to be bulk sensitive due to the small root mean square displacement of below 1 μm (see Table S2) in comparison to the large grain size of several hundred μm as seen in the SEM (Figure 1). Extrapolation from the high temperature values using the activation energy and assuming Arrhenius behavior yield room temperature diffusion coefficients of $6.2 \cdot 10^{-13}$ and $6.5 \cdot 10^{-15}$ for Ga-LLZO and Al-LLZO, respectively.

At the same time as PFG-NMR, ^{7}Li spin-lattice relaxation (T_1) NMR experiments were measured for a wider temperature range from 453 K to 300 K and the activation energy was extracted (Figure S5). ^{7}Li T_1 measurements gave an even lower value for the activation energy of Ga-doped LLZO (E_a = 0.094 eV), which is attributed to the fact that this technique is highly sensitive to local ion hopping, such as the rapid oscillation over the low energy barrier between the adjacent Li 94h split sites with 48g in the middle (octahedral) or site jumps (octahedral-tetrahedral or octahedral-octahedral).[39,40] This low activation energy shows that Ga-LLZO possesses low activation barriers for local ion hopping, in line with the overall low bulk diffusion behavior.

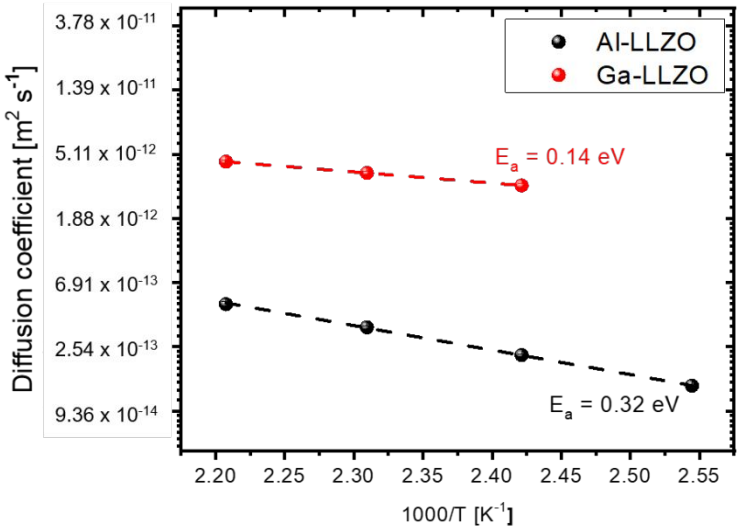

Figure 8. Variable temperature ^{7}Li PFG-NMR performed on Al-LLZO and Ga-LLZO powders, higher activation energies for the Al-doped sample for Li ion diffusion. Good agreement is observed between the ^{7}Li PFG NMR and the bulk E_a value experimentally calculated from EIS.

In order to confirm a consistent behaviour of our Ga-LLZO samples, different samples in different configurations (including Li/LLZO/Li, Au/LLZO/Au symmetrical cells) were tested; Table S3 shows the values of E_a calculated for these samples and the typical average values for the different components in three common Li/LLZO/Li configurations are reported in Figure 9.

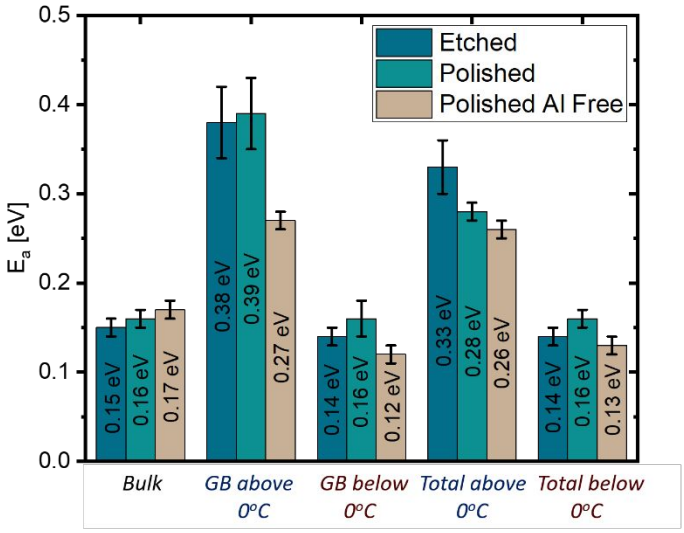

Figure 9: Activation energy values extracted from the Arrhenius plots for different kind of Ga-LLZO samples.

As shown in Figure 9, an Al-free pellet was synthesised in a MgO crucible and measured in order to assess the effect that Al segregated at the grain boundaries could have on the grain boundary activation energy. It can be noted that for the Al-free pellet, the grain boundary E_a above 0 °C is significantly lower than the values reported for the pellets sintered in Al_2O_3 crucibles. The lower activation energy for Al-free grain boundaries suggests that Al makes ion hopping energetically more difficult and that avoidance of Al during the processing of garnets would be desirable to facilitate Li conduction in both bulk and grain boundaries.

In order to understand what is promoting the change in the electrical behaviour of the grain boundaries, time-of-flight secondary ion mass spectrometry (TOF-SIMS) was performed on our samples. We found that both Ga and Al segregate in the grain boundaries (Figure S7), probably forming a glassy-type phase that is responsible for the electrochemical performance. We plan to report on dopant segregation at the grain boundaries elsewhere.[41] This phase segregation would also explain the low capacitance obtained for the grain boundary process and the variability of results in the literature for grain boundary contributions in garnets, since different dopants and processing methods would lead to different grain boundary composition and performance. As previously reported, Al tends to concentrate at the grain boundaries of LLZO as a result of liquid-phase sintering,[12,42] promoted by the diffusion of Al from Al_2O_3 crucibles. It is observed in this study that Ga also tends to preferentially segregate in the grain boundaries. The reason behind the change in activation energy at 0 °C could be related to a reversible phase occurring in the Li-Ga-O ternary system at the grain boundaries.

We propose that the combination of Al and Ga which can segregate at the grain boundaries could play a pivotal role in the ion hopping mechanism of this materials and we show that by tuning the grain boundary composition we can radically change the electrical properties of garnet electrolytes. This is important because by controlling the grain boundary conductivity we can improve the current distribution and improve the stability of garnet electrolytes in contact with Li anode

electrodes, a major industrial challenge for the development of high energy density fast changing devices.

The total activation energy value of Ga-LLZO above 0 °C that we calculated from EIS measurements (0.38 eV) agrees with data previously reported in the literature,[43,44] but an activation energy value below 0 °C has not often been reported. In 2014, Tenhaeff *et al.* reported an E_a of 0.4 eV for Al-LLZO; however, they did not observed a change of activation energy in the temperature range -100 to +60 °C.[30] It is worth noting that the sample used in their study was prepared by solid-state synthesis and boron nitride was used to prevent reaction of the pellets with the Al_2O_3 crucibles during sintering. In 2011, Buschmann *et al.* also reported the activation energy for several Al-LLZO pellets (0.34-0.49 eV) and did not observe any change in activation energy below 0 °C.[45] In their study, they also used Al-free crucibles. In our study we use Al_2O_3 crucibles during the thermal treatments of our pellets as described in the experimental section. In order to validate our results, a variable temperature EIS study was also carried out on an Al-LLZO pellet with microstructure and density comparable with the Ga-doped pellets used in this study. In accordance with the studies described above, we also did not observe a change in activation energy for the Al-doped sample (Figure S6) proving that the co-segregation of Al and Ga plays a pivotal role on the grain boundaries transport properties.

Conclusions

In this work we have carried out a systematic electrochemical impedance analysis of Ga-LLZO in order to assign and separate the contributions of bulk, grain boundary and interfacial processes. EIS spectra show a superimposition of the bulk and grain boundary contributions in samples with grain sizes of >300 μm in which a segregation of Ga and Al dopants and Li is observed at the grain boundaries. The identification of the different processes was possible by measuring impedance in a wide temperature range of +75 to -100 °C. Distribution of relaxation times analysis also confirmed these assignments. A low bulk activation energy of 0.14 (± 0.01) eV for Li conduction has been proven by means of impedance analysis and NMR diffusivity while NMR relaxometry confirms fast

local ion motion in the bulk. This is the lowest activation energy reported so far for Li in garnet electrolytes and can be ascribed to a coherent distinction between bulk and grain boundary processes measured in samples with minimal moisture reactivity. The study also suggests that the total conductivity is dominated by the grain boundary resistance which can be tuned by varying its composition. Grain boundary conductivity is controlled by the segregation of dopants and it is shown that by adjusting the amount and species of dopant at the grain boundaries, it is possible to control the E_a of Ga-LLZO and, as such, allow a targeted engineering of this material. This study therefore paves the way to new design strategies for garnet electrolytes, for improvement of fast current distribution upon cycling by influencing the transport properties of the grain boundaries in the garnet electrolyte.

Experimental section

Synthesis, Structural and Microstructural Characterisation of Ga-LLZO

LLZO pellets with the nominal composition $Li_{6.55}Ga_{0.15}La_3Zr_2O_{12}$ were synthesised *via* a sol-gel route using $LiNO_3$ anhydrous (99.0%, Alfa Aesar), La_2O_3 (99.9%. Sigma Aldrich), $Zr(C_5H_7O_2)_4$ (97%, Sigma Aldrich) and Ga_2O_3 (99.999%, Alfa Aesar) as starting precursors. The precursors were weighted in the desired stoichiometry in plastic weighing boats and dissolved in a 9:1 mixture of ~0.5 M citric acid (ACS reagent, ≥99.5%, Sigma Aldrich) and nitric acid (68%, VWR). The resulting gel was combusted at 600 ^oC for 12h with heating and cooling ramps of 2 $^oC\ min^{-1}$ and 10 $^oC\ min^{-1}$ respectively. The as obtained powders were transferred in an Ar filled glove box when still at a temperature above 100 ^oC to avoid any uptake of moisture, and manually milled to obtain a fine powder. Calcination was carried out on the powders in Al_2O_3 crucibles (apart from Al-free LLZO, where MgO crucibles were used) using a tubular furnace connected to a dry O_2 cylinder (BOC high purity grade N6.0) at 800 ^oC for 12h with a heating and cooling ramp of 5 $^oC\ min^{-1}$. The calcined powders were transferred back to the Ar filled glove box and manually milled again to obtain a fine powder that was pressed in pellets of 10mm diameter under 2 tons for 1 minute. The green body pellets were then fully covered in mother powder and sintered in Al_2O_3 crucibles at 1150 ^oC in an Ar

filled furnace connected to the glove box and kept at 3 hPa of pressure. The sintered pellets were finely polished using SiC paper up to 4000 grit (5 μm) and thermally etched at 900 ^{o}C for 30 minutes in the Ar filled furnace. The density of the pellets was calculated geometrically for each set of samples by measuring volume and mass of each pellet and normalising by the theoretical density of 5.02 g/cm^{3}. The typical dimension of the pellets was 8mm in diameter and 1mm in thickness. A control sample was kept for each synthesis in order to structurally and microstructurally characterise each batch of samples. X-Ray Diffraction was carried out using a Bruker D2 Phaser instrument with a 2θ range of 10^{o} to 80^{o}, a step size of 0.034^{o} 2θ and a time step of 2 s step^{-1}. Rietveld refinement of the X-ray diffraction patterns was carried out using Fullprof Suite software. SEM images were recorded using a Zeiss electron microscope (Leo Gemini 1525 field emission gun) with accelerating voltage of 5keV.

Electrochemical Analysis

Symmetrical Li/LLZO/Li cells were prepared by cold pressing freshly scraped Li metal foils with a diameter of 6mm on both sides of the pellets in an Ar filled glove box right after thermal etching. Symmetrical Au/LLZO/Au cells were prepared by masking the LLZO pellets and sputtering gold with a diameter of 6 mm. The sandwiched pellets were assembled in commercial 2032 coin cell cases using SS spacers and a spring in order to secure the sample inside the coin cell and provide a constant pressure calculated to be 1 MPa for 1 mm thick pellets. Electrochemical Impedance Spectroscopy was carried out in the range 13 MHz – 1 Hz at 20 mV signal amplitude using a Solartron 1260 Frequency Response Analyser. The temperature was kept constant using a Linkam HFS600E-P stage; prior to any measurement the cells were kept at the set temperature for 1.5 hours in order to avoid any temperature gradient within the thickness of the pellet. Nyquist-type plots were analysed and fitted using Z-view software. Kramers-Kronig validity test was performed prior to fit the data using Lin-KK tool developed at KIT.

Distribution of Relaxation Times Analysis

The distribution of relaxation times (DRT) analysis was carried out with an in-house code which is an improved variation of the classical Tikhonov regularisation method. The DRT code applies a singular value decomposition and extends the frequency range beyond the frequencies experimentally measured so that the distribution function of these additional frequencies damps the divergent behaviour of Tikhonov regularisation for incomplete impedance spectra (i.e., experimental EIS data whose imaginary component does not approach zero at high or low frequency). A complete description of the DRT code, along with validation and comparison with other DRT approaches, is reported elsewhere.[46]

Solid State NMR Measurements

Powder samples of different LLZO compositions (Ga-, Ge- and undoped LLZO) were sent in Ar-filled, sealed containers which were later transferred under Ar to 5 mm NMR glass tubes modified with a J. Young valve, making the total volume of the powders in the container around 200 to 400 µl. All spectra were recorded on a Bruker Avance III 300 MHz spectrometer using a Diff50 probehead equipped with an extended variable temperature (EVT) 5 mm single-tuned ^{7}Li saddle coil insert. The π/2 pulse length of approx. 7-8 µs was optimized on the sample.

Diffusion spectra were recorded with a stimulated echo pulsed field gradient (PFG) sequence at elevated temperatures due to the increase in T_2 observed at high temperature. (*N.B.* No attempt was made to calibrate the temperature for this experimental setup because a single-tuned ^{7}Li coil was used and no reliable ^{7}Li reference is routinely used for temperature calibration. The Bruker manual states that for static measurements, the temperature calibration should be within ±7 degrees of the set value.) The increase in T_2 allowed the use of longer gradient pulses, δ, that were necessary to measure the relatively slow diffusion coefficients present in the solid electrolytes. The gradient strength, g, was varied from 0.87 to 2300 G·cm^{-1}. The response of the NMR signal intensity, I, to variation in gradient strength, g, is described by the Stejskal–Tanner equation (Equation 4):

$$\frac{I}{I_0} = exp\left(-g^2\gamma^2\delta^2\left(\Delta - \frac{\delta}{3}\right) \cdot D \right) \quad \text{Equation 4}$$

where I_0 is the intensity in the absence of gradients, γ is the gyromagnetic ratio ($\gamma_{^7Li} = 103.962 \times 10^6 \cdot s^{-1} \cdot T^{-1}$), δ is the effective gradient pulse duration, Δ is the diffusion time, and D is the diffusion coefficient. Typical δ values ranged from 0.8 ms to 1.5 ms and Δ values ranged from 60–150 ms.

For Ga-LLZO, ^{7}Li diffusivities were measured over the temperature range of 413-453 K. For the (undoped) Al-LLZO sample, ^{7}Li diffusivities were measured over the temperature range of 393-453 K.

T_1 relaxation times were measured using the same setup as described above in the range of 300-450 K for Ga-LLZO samples. Spectra were recorded using a standard 180-τ-90 inversion recovery pulse sequence and analyzed in TopSpin with the integrated NMR Relaxation Guide. The integral intensity for each delay (τ) was fitted to the appropriate inbuilt function to obtain the values for T_1 (Equation 5):

$$\frac{I(\tau)}{I_0} = 1 - 2 \cdot A \cdot exp\left(-\frac{\tau}{T_1}\right) \qquad \text{Equation 5}$$

Here, τ is the delay between the two pulses, I_0 is the intensity when fully relaxed (i.e. infinite τ), $I(\tau)$ is the intensity measured for the corresponding delay, while A is the preexponential factor, which is ideally equal to 1.

Acknowledgment

This work was funded by the EPSRC grants EP/P003532/1 and ICSF EP/R024006/1 and by the European Commission grant FETPROACT-2018-2020 “HARVERSTORE” 824072. L.E.M. acknowledges support from a Marie Skłodowska-Curie Postdoctoral Fellowship and the Charles and Katharine Darwin Research Fellowship. S.P.E. was funded via an EPSRC iCASE (Award 1834544) and via the Royal Society (RP\R1\180147).

Author Information

Corresponding Authors

*f.pesci@imperial.ac.uk, a.aguadero@imperial.ac.uk

Author Contributions

All authors have given approval to the final version of the manuscript.

Associated Content

Supporting information. Ga-LLZO XRD pattern, Kramers-Kronig validity test, DRT analysis of variable temperature EIS spectra, Fitting results of variable temperature spectra, E_a of interfacial processes, Spin-lattice NMR relaxation measurements for LLZO powders, extended PFG-NMR analysis, Arrhenius-type plot for Al-LLZO, ToF-SIMS maps. This material is available free of charge via the Internet at http://pubs.acs.org.

Bibliography

(1) Janek, J.; Zeier, W. G. A Solid Future for Battery Development. *Nat. Energy* **2016**, *1* (9), 16141. https://doi.org/10.1038/nenergy.2016.141.

(2) Yao, X.; Liu, D.; Wang, C.; Long, P.; Peng, G.; Hu, Y. S.; Li, H.; Chen, L.; Xu, X. High-Energy All-Solid-State Lithium Batteries with Ultralong Cycle Life. *Nano Lett.* **2016**, *16* (11), 7148–7154. https://doi.org/10.1021/acs.nanolett.6b03448.

(3) Kato, Y.; Hori, S.; Saito, T.; Suzuki, K.; Hirayama, M.; Mitsui, A.; Yonemura, M.; Iba, H.; Kanno, R. High-Power All-Solid-State Batteries Using Sulfide Superionic Conductors. *Nat. Energy* **2016**, *1* (March), 16030. https://doi.org/10.1038/nenergy.2016.30.

(4) Zhu, Y.; He, X.; Mo, Y. Origin of Outstanding Stability in the Lithium Solid Electrolyte Materials: Insights from Thermodynamic Analyses Based on First-Principles Calculations. *ACS Appl. Mater. Interfaces* **2015**, *7* (42), 23685–23693. https://doi.org/10.1021/acsami.5b07517.

(5) Junji Awaka, Norihito Kijima, Hiroshi Hayakawa, J. A. Synthesis and Structure Analysis of Tetragonal $Li_7La_3Zr_2O_{12}$ with the Garnet-Related Type Structure. *J. Solid State Chem.* **2009**, *182*, 2046–2052.

(6) Rangasamy, E.; Wolfenstine, J.; Sakamoto, J. The Role of Al and Li Concentration on the Formation of Cubic Garnet Solid Electrolyte of Nominal Composition $Li_7La_3Zr_2O_{12}$. *Solid State Ionics* **2012**, *206*, 28–32. https://doi.org/10.1016/j.ssi.2011.10.022.

(7) Bernuy-Lopez, C.; Manalastas, W.; Lopez del Amo, J. M.; Aguadero, A.; Aguesse, F.; Kilner, J. A. Atmosphere Controlled Processing of Ga-Substituted Garnets for High Li-Ion Conductivity Ceramics. *Chem. Mater.* **2014**, *26* (12), 3610–3617. https://doi.org/10.1021/cm5008069.

(8) Nakayama, M.; Kotobuki, M.; Munakata, H.; Nogami, M.; Kanamura, K. First-Principles Density Functional Calculation of Electrochemical Stability of Fast Li Ion Conducting Garnet-Type Oxidesw. *Phys. Chem. Chem. Phys* **2012**, *14*, 10008–10014. https://doi.org/10.1039/c2cp40634a.

(9) Samson, A. J.; Hofstetter, K.; Bag, S.; Thangadurai, V. A Bird's-Eye View of Li-Stuffed Garnet-Type Li7La3Zr2O12 Ceramic Electrolytes for Advanced All-Solid-State Li Batteries. *Energy and Environmental Science*. Royal Society of Chemistry October 1, 2019, pp 2957–2975. https://doi.org/10.1039/c9ee01548e.

(10) Zhao, N.; Khokhar, W.; Bi, Z.; Shi, C.; Guo, X.; Fan, L. Z.; Nan, C. W. Solid Garnet Batteries. *Joule*. Cell Press May 15, 2019, pp 1190–1199. https://doi.org/10.1016/j.joule.2019.03.019.

(11) Sharafi, A.; Kazyak, E.; Davis, A. L.; Yu, S.; Thompson, T.; Siegel, D. J.; Dasgupta, N. P.; Sakamoto, J. Surface Chemistry Mechanism of Ultra-Low Interfacial Resistance in the Solid-State Electrolyte $Li_7La_3Zr_2O_{12}$. *Chem. Mater.* **2017**, *29* (18), 7961–7968. https://doi.org/10.1021/acs.chemmater.7b03002.

(12) Pesci, F. M.; Brugge, R. H.; Hekselman, A. K. O.; Cavallaro, A.; Chater, R. J.; Aguadero, A. Elucidating the Role of Dopants in the Critical Current Density for Dendrite Formation in Garnet Electrolytes. *J. Mater. Chem. A* **2018**, *6* (40), 19817–19827. https://doi.org/10.1039/C8TA08366E.

(13) Flatscher, F.; Philipp, M.; Ganschow, S.; Martin, H.; Wilkening, R.; Rettenwander, D. The Natural Critical Current Density Limit for $Li_7La_3Zr_2O_{12}$ Garnets. *J. Mater. Chem. A* **2020**, Advance Article. https://doi.org/10.1039/c9ta14177d.

(14) Cheng, L.; Crumlin, E. J.; Chen, W.; Qiao, R.; Hou, H.; Lux, S. F.; Zorba, V.; Russo, R.; Kostecki, R.; Liu, Z.; Persson, K.; Yang, W.; Cabana, J.; Richardson, T.; Chen, G.; Doeff, M. The Origin of High Electrolyte–Electrode Interfacial Resistances in Lithium Cells Containing Garnet Type Solid Electrolytes. *Phys. Chem. Chem. Phys.* **2014**, *16* (16), 18294–18300. https://doi.org/10.1039/c4cp02921f.

(15) Cheng, L.; Liu, M.; Mehta, A.; Xin, H. L.; Lin, F.; Persson, K. A.; Chen, G.; Crumlin, E. J.; Doeff, M. M. Garnet Electrolyte Surface Degradation and Recovery. *ACS Appl. Energy Mater.* **2018**, *1*, 7244–7252. https://doi.org/10.1021/acsaem.8b01723.

(16) Sharafi, A.; Yu, S.; Naguib, M.; Lee, M.; Ma, C.; Meyer, H. M.; Nanda, J.; Chi, M.; Siegel, D. J.; Sakamoto, J. Impact of Air Exposure and Surface Chemistry on Li-$Li_7La_3Zr_2O_{12}$ Interfacial Resistance. *J. Mater. Chem. A* **2017**, *5* (26), 13475–13487. https://doi.org/10.1039/C7TA03162A.

(17) Han, X.; Gong, Y.; Fu, K. (Kelvin); He, X.; Hitz, G. T.; Dai, J.; Pearse, A.; Liu, B.; Wang, H.; Rubloff, G.; Mo, Y.; Thangadurai, V.; Wachsman, E. D.; Hu, L. Negating Interfacial Impedance in Garnet-Based Solid-State Li Metal Batteries. *Nat Mater* **2017**, *16* (5), 572–579.

(18) Wang, M. J.; Choudhury, R.; Sakamoto, J. Characterizing the Li-Solid-Electrolyte Interface Dynamics as a Function of Stack Pressure and Current Density. *Joule* **2019**, *3* (9), 2165–2178. https://doi.org/10.1016/J.JOULE.2019.06.017.

(19) Kasemchainan, J.; Zekoll, S.; Spencer Jolly, D.; Ning, Z.; Hartley, G. O.; Marrow, J.; Bruce, P. G. Critical Stripping Current Leads to Dendrite Formation on Plating in Lithium Anode Solid Electrolyte Cells. *Nat. Mater.* **2019**, *18* (10), 1105–1111. https://doi.org/10.1038/s41563-019-0438-9.

(20) Krauskopf, T.; Hartmann, H.; Zeier, W. G.; Janek, J. Toward a Fundamental Understanding of the Lithium Metal Anode in Solid-State Batteries—An Electrochemo-Mechanical Study on the Garnet-Type Solid Electrolyte $Li_{6.25}Al_{0.25}La_3Zr_2O_{12}$. *ACS Appl. Mater. Interfaces* **2019**, *11* (15), 14463–14477. https://doi.org/10.1021/acsami.9b02537.

(21) Jeff Sakamoto. More Pressure Needed. *Nat. Energy* **2019**, *4*, 827–828.

(22) Brugge, R. H.; Hekselman, A. K. O.; Cavallaro, A.; Pesci, F. M.; Chater, R. J.; Kilner, J. A.; Aguadero, A. Garnet Electrolytes for Solid State Batteries: Visualisation of Moisture-Induced Chemical Degradation and Revealing Its Impact on the Li-Ion Dynamics. *Chem. Mater.* **2018**,

30 (11), 3704–3713.

(23) Huo, H.; Chen, Y.; Zhao, N.; Lin, X.; Luo, J.; Yang, X.; Liu, Y.; Guo, X.; Sun, X. In-Situ Formed Li_2CO_3-Free Garnet/Li Interface by Rapid Acid Treatment for Dendrite-Free Solid-State Batteries. *Nano Energy* **2019**, *61*, 119–125. https://doi.org/10.1016/j.nanoen.2019.04.058.

(24) Huo, H.; Luo, J.; Thangadurai, V.; Guo, X.; Nan, C.-W.; Sun, X. Li_2CO_3 : A Critical Issue for Developing Solid Garnet Batteries. **2020**, *11*, 46. https://doi.org/10.1021/acsenergylett.9b02401.

(25) Luo, W.; Gong, Y.; Zhu, Y.; Li, Y.; Yao, Y.; Zhang, Y.; Fu, K. K.; Pastel, G.; Lin, C.-F.; Mo, Y.; Wachsman, E. D.; Hu, L. Reducing Interfacial Resistance between Garnet-Structured Solid-State Electrolyte and Li-Metal Anode by a Germanium Layer. *Adv. Mater.* **2017**, *29* (22), 1606042. https://doi.org/10.1002/adma.201606042.

(26) Krauskopf, T.; Mogwitz, B.; Rosenbach, C.; Zeier, W. G.; Janek, J. Diffusion Limitation of Lithium Metal and Li–Mg Alloy Anodes on LLZO Type Solid Electrolytes as a Function of Temperature and Pressure. *Adv. Energy Mater.* **2019**. https://doi.org/10.1002/aenm.201902568.

(27) Rettenwander, D.; Redhammer, G.; Preishuber-Pflügl, F.; Cheng, L.; Miara, L.; Wagner, R.; Welzl, A.; Suard, E.; Doeff, M. M.; Wilkening, M.; Fleig, J.; Amthauer, G. Structural and Electrochemical Consequences of Al and Ga Cosubstitution in $Li_7La_3Zr_2O_{12}$ Solid Electrolytes. *Chem. Mater.* **2016**, *28* (7), 2384–2392. https://doi.org/10.1021/acs.chemmater.6b00579.

(28) Zhang, L.; Chen, P.; Hu, Z. Synthesis of Nano-Scale Fast Ion Conducting Cubic $Li_7La_3Zr_2O_{12}$. *Nanotechnology* **2013**, *24*, 424005. https://doi.org/10.1088/0957-4484/24/42/424005.

(29) Murugan, R.; Thangadurai, V.; Weppner, W. Fast Lithium Ion Conduction in Garnet-Type $Li_7La_3Zr_2O_{12}$. *Angew. Chemie - Int. Ed.* **2007**, *46* (41), 7778–7781. https://doi.org/10.1002/anie.200701144.

(30) Tenhaeff, W. E.; Rangasamy, E.; Wang, Y.; Sokolov, A. P.; Wolfenstine, J.; Sakamoto, J.; Dudney, N. J. Resolving the Grain Boundary and Lattice Impedance of Hot-Pressed $Li_7La_3Zr_2O_{12}$ Garnet Electrolytes. *ChemElectroChem* **2014**, *1*, 375–378. https://doi.org/10.1002/celc.201300022.

(31) Irvine, J. T. S.; Sinclair, D. C.; West, A. R. Electroceramics: Characterization by Impedance Spectroscopy. *Adv. Mater.* **1990**, *2* (3), 132–138. https://doi.org/10.1002/adma.19900020304.

(32) Schichlein, H.; Müller, A. C.; Voigts, M.; Krügel, A.; Ivers-Tiffée, E. Deconvolution of Electrochemical Impedance Spectra for the Identification of Electrode Reaction Mechanisms in Solid Oxide Fuel Cells. *J. Appl. Electrochem.* **2002**, *32*, 875–882. https://doi.org/10.1023/A:1020599525160.

(33) Wan, T. H.; Saccoccio, M.; Chen, C.; Ciucci, F. Influence of the Discretization Methods on the Distribution of Relaxation Times Deconvolution: Implementing Radial Basis Functions with DRTtools. *Electrochim. Acta* **2015**, *184*, 483–499. https://doi.org/10.1016/j.electacta.2015.09.097.

(34) Rietveld, H. M. A Profile Refinement Method for Nuclear and Magnetic Structures. *J. Appl. Crystallogr.* **1969**, *2* (2), 64-71. https://doi.org/10.1107/s0021889869006558.

(35) Stoller, M. D.; Stoller, S. A.; Quarles, N.; Suk, J. W.; Murali, S.; Zhu, Y.; Zhu, X.; Ruoff, R. S. Using Coin Cells for Ultracapacitor Electrode Material Testing. *J. Appl. Electrochem.* **2011**, *41*, 681–686. https://doi.org/10.1007/s10800-011-0280-5.

(36) Boukamp, B. A. A Linear Kronig-Kramers Transform Test for Immittance Data Validation. *J. Electrochem. Soc* **1995**, *142* (6), 1885–1894.

(37) Schönleber, M.; Klotz, D.; Ivers-Tiffée, E. A Method for Improving the Robustness of Linear Kramers-Kronig Validity Tests. *Electrochim. Acta* **2014**, *131*, 20–27. https://doi.org/10.1016/j.electacta.2014.01.034.

(38) Kramers-Kronig Validity Test Lin-KK for Impedance Spectra.

https://www.iam.kit.edu/wet/english/Lin-KK.php.

(39) Jalem, R.; Yamamoto, Y.; Shiiba, H.; Nakayama, M.; Munakata, H.; Kasuga, T.; Kanamura, K. Concerted Migration Mechanism in the Li Ion Dynamics of Garnet-Type $Li_7La_3Zr_2O_{12}$. **2013**. https://doi.org/10.1021/cm303542x.

(40) Uitz, M.; Epp, V.; Patrick Bottke, ·; Wilkening, · Martin; Wilkening, M. Ion Dynamics in Solid Electrolytes for Lithium Batteries Probing Jump Rates and Activation Energies through Time-Domain Li NMR. **2017**, *38*, 142–156. https://doi.org/10.1007/s10832-017-0071-4.

(41) Brugge, R. H.; Pesci, F. M.; Cavallaro, A.; Sole, C. G.; Isaacs, M.; Weatherup, R. S.; Kerherve, G.; Aguadero, A. The Origin of Chemical Inhomogeneity in Garnet Electrolytes and Its Impact on Electrochemical Performance. *Unpublished Experiments*

(42) Cheng, L.; Park, J. S.; Hou, H.; Zorba, V.; Chen, G.; Richardson, T.; Cabana, J.; Russo, R.; Doeff, M. Effect of Microstructure and Surface Impurity Segregation on the Electrical and Electrochemical Properties of Dense Al-Substituted $Li_7La_3Zr_2O_{12}$. *J. Mater. Chem. A* **2014**, *2* (1), 172–181. https://doi.org/10.1039/C3TA13999A.

(43) Wu, J. F.; Chen, E. Y.; Yu, Y.; Liu, L.; Wu, Y.; Pang, W. K.; Peterson, V. K.; Guo, X. Gallium-Doped $Li_7La_3Zr_2O_{12}$ Garnet-Type Electrolytes with High Lithium-Ion Conductivity. *ACS Appl. Mater. Interfaces* **2017**, *9* (2), 1542–1552. https://doi.org/10.1021/acsami.6b13902.

(44) Rettenwander, D.; Redhammer, G.; Preishuber-Pflügl, F.; Cheng, L.; Miara, L.; Wagner, R.; Welzl, A.; Suard, E.; Doeff, M. M.; Wilkening, M.; Fleig, J.; Amthauer, G. Structural and Electrochemical Consequences of Al and Ga Cosubstitution in $Li_7La_3Zr_2O_{12}$ Solid Electrolytes. *Chem. Mater.* **2016**, *28* (7), 2384–2392. https://doi.org/10.1021/acs.chemmater.6b00579.

(45) Buschmann, H.; Dölle, J.; Berendts, S.; Kuhn, A.; Bottke, P.; Wilkening, M.; Heitjans, P.; Senyshyn, A.; Ehrenberg, H.; Lotnyk, A.; Duppel, V.; Kienle, L.; Janek, J. Structure and Dynamics of the Fast Lithium Ion Conductor "$Li_7La_3Zr_2O_{12}$." *Phys. Chem. Chem. Phys.* **2011**, *13* (43), 19378. https://doi.org/10.1039/c1cp22108f.

(46) Clematis, D.; Ferrari, T.; Bertei, A.; Nicolella, C.; Carpanese, M. P.; Asensio, A. M.; Viviani, M.; Presto, S.; Barbucci, A. On the Stabilization and Extension of the Distribution of Relaxation Times Analysis. *Unpublished Experiments*

Table of Content